High Valence Binary Metal-Organic Framework as Electrode Material for Aqueous Asymmetric Supercapacitor

T. B. Naveen,[a] D. Durgalakshmi*,[b] S. Balakumar[c] and R. Ajay Rakkesh*[a]

[a]Functional Nano-Materials (FuN) Laboratory, Department of Physics and Nanotechnology, Faculty of Engineering and Technology, SRM Institute of Science and Technology, Kattankulathur – 603203, TN, India.

[b]Department of Medical Physics, Anna University, Chennai – 600 025, TN, India

[c]National Centre for Nanoscience and Nanotechnology, University of Madras, Chennai – 600 025, TN, India

*Corresponding author: ajayr1@srmist.edu.in; ajayrakkesh@gmail.com; durgaklakshmi@gmail.com

Experimental

Materials:

The precursors such as Nickel (II) chloride hexahydrate ($NiCl_2.6H_2O$) extrapure 99%, Cobalt (II) chloride hexahydrate ($CoCl_2.6H_2O$) extrapure AR and Terepthalic acid 98% was procured from SRL India, while the solvent N, N-Dimethylformamide (DMF) obtained from RANKEM India. Also, rGO derived from coconut shell biomass has been utilized for fabricating asymmetric supercapacitor setup.

Synthesis of Ni-BDC and NiCo-BDC nanosheets:

To begin with the synthesis process, firstly the $NiCl_2.6H_2O$ and terepthalic acid was weighed accurately based on molar ratio of 1:1. Then the weighed $NiCl_2.6H_2O$ and terepthalic acid were dissolved separately by using 40 ml of DMF for each. After well dissolved solution is observed, the two solutions were mixed by adding metal precursor dropwise on to the beaker containing terepthalic acid. The mixture was stirred using magnetic stirrer for an hour, after that the solution (80 ml) was transferred to a Teflon-lined stainless-steel autoclave (100 ml) and subjected to 140°C for 12 hours and allowed cool naturally, then the sample was centrifuged and washed with ethanol and distilled water for several times to get rid off impurities. The sample is then dried at 80°C for 12 hrs. to obtain powder. The same procedure is followed for the synthesis of NiCo-BDC, where the precursors $NiCl_2.6H_2O$, $CoCl_2.6H_2O$ and terepthalic acid were taken in molar ratio of 1:1:2 (shown in **Fig.S1**).
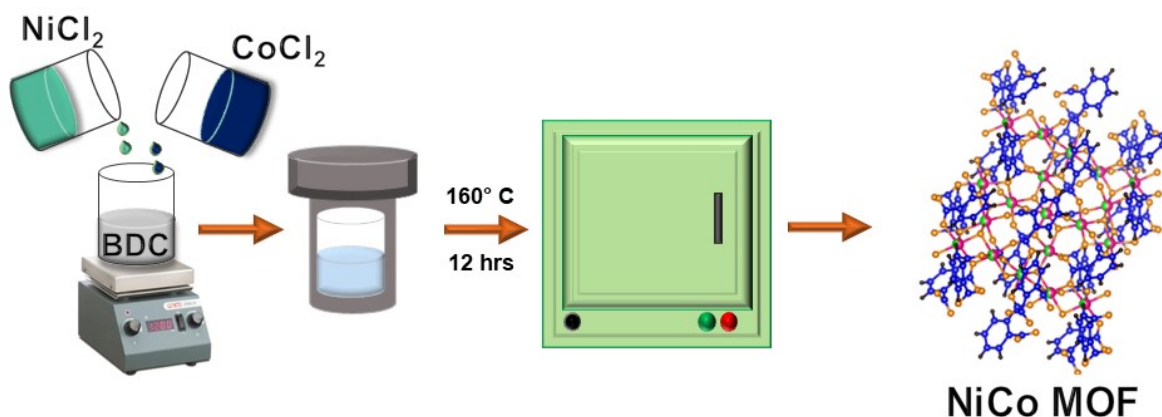
Fig S1. Portrays the strategy carried out for synthesis of Ni /NiCo-BDC.

Characterizations

The obtained MOFs were analyzed and characterized using various techniques. X-ray powder diffraction (XRD) was performed using a PANalytical powder diffractometer with Copper Kα radiation for confirming the crystal structure present. Fourier transform infrared spectroscopy (FTIR) was conducted using a SHIMADZU, IR TRACER 100 spectrometer, covering an IR range from 4000 to 400 cm^{-1}. Raman spectroscopy was carried out using a Horiba LabRAM HR evolution instrument, employing laser light of 532 nm and recording data within the range of 400 to 1800 cm^{-1}. The surface chemical analysis was studied with X-ray photoelectron spectroscopy using PHI-VERSAPROBE III. The morphology and elemental analysis of the sample were observed using high-resolution scanning electron microscopy (HRSEM) with a Thermoscientific Apreo S instrument. The specific surface area using N2 adsorption-desorption measurements employing the Brunauer–Emmett–Teller (BET) method was investigated with a Micromeritics ASAP 2020 surface area analyser.

The electrochemical behaviour of Ni-BDC and NiCo-BDC nanosheets was investigated through various electrochemical characterization techniques including cyclic voltammetry (CV), galvanostatic charge-discharge (GCD), and electrochemical impedance spectroscopy (EIS). The measurements were performed using an OrigaFlex OGF05A electrochemical workstation with a three-electrode system. Platinum wire and Ag/AgCl were employed as the counter and reference electrodes, respectively. To prepare the working electrode, a mixture comprising 90 wt.% of the active material along with 5 wt.% of PVDF (polyvinyldene fluoride) and 5% carbon black as binding agent and conductive additive was thoroughly mixed using N-Methyl-2-pyrrolidone (NMP) as solvent until a slurry like texture is achieved. The slurry was

simply coated on nickel foam (NF) by using simple brushing technique on area of 0.5 x 0.5 cm. The nickel foam was initially weighed before coating, denoted as 'E$_w$'. Subsequently, after the coating dried, the electrodes were reweighed and labeled as 'E$_{cw}$'. The weight of the active materials coated was determined by subtracting E$_w$ from E$_{cw}$.

For the electrochemical testing, an electrolyte consisting of 3M potassium hydroxide (KOH)) was used. The rGO was also subjected to electrochemical studies using a three-electrode setup in the potential range of -1.2 to 0V before moving into fabrication of asymmetric supercapacitor. The specific capacitance (C$_S$) was calculated using the formula:

$$C_S = \frac{I\Delta t_d}{m(\Delta V)},$$ ----(1)

In this context, 'I' stands for the current used in the discharge process, 'Δt_d' indicates the duration of discharge, 'm' represents the mass of the active substance on the electrode, and 'ΔV' signifies the range of potential for the material. While for two electrode setup 'm' represents total mass of active material on both the electrodes.

The equation $i_p = av^b$ transformed to $\log(i_p) = \log(a) + b\log(v)$, were used by researchers to determine the current contribution by finding b-value (slope) from plot between $\log(i_p)$ and $\log(v)$ where 'i_p' is peak anodic/cathodic current and 'v' is scan rate. The b-value generally lies between 0.5 to 1 and for values near to 0.5 the current contribution is dominated by diffusion controlled faradaic process where as values near 1 were related to capacitive controlled current.[1,2]

Fabrication and testing of aqueous asymmetric supercapacitor:

The aqueous asymmetric supercapacitor (AASC) basically a two-electrode setup was fabricated using NiCo-BDC/NF as anode and rGO/NF as cathode in 3M KOH solution (as shown in Fig S12) was packed into a pouch to form the device, whose electrochemical behaviour was studied with the aforementioned characterization techniques for potential range of 0 to 1.6V. For obtaining maximum output from the AASC there needs to be a charge balance between two electrodes ($q^+ = q^-$) which depends on the mass loading (m^+/m^-). The specific capacitance of rGO and NiCo-BDC obtained using three electrode setup was used to determine the optimum mass ratio of positive and negative electrode materials. The mass ratio was calculated using the following equation:

$$\frac{m^+}{m^-} = \frac{C^-\Delta V^-}{C^+\Delta V^+}$$

Where C^- and C^+ are specific capacitance; ΔV^- and ΔV^+ are the potential window of rGO and NiCo-BDC respectively.

Energy Density (Wh/Kg):

$$E = \frac{1}{2}C_S\Delta V^2 \qquad\qquad \text{----(2)}$$

Power Density (W/Kg):

$$P = \frac{E}{\Delta t_d} \qquad\qquad \text{----(3)}$$

Coulombic efficiency:

$$\eta = \frac{\Delta t_d}{\Delta t_c} \qquad\qquad \text{----(4)}$$

Where, ΔV represents the operating voltage (V), Δt_d (s) represents the discharge time, and Δt_c represents the charging time.[3-6]

BET Analysis:

The specific surface area (SSA) and pore size measurements assessed through BET analysis using nitrogen adsorption–desorption isotherms. Pore size distribution (PSD) was determined using the Barrett–Joyner–Halenda (BJH) method (Shown in Fig. S6a&b). The calculated BET SSA is of 29.813 m^2g^{-1}. The standard isotherm indicates that the MOFs possess both micropores and mesopores, where the majority lies in the mesoporous region (~35 nm). The NiCo-BDC exhibits a typical type IV isotherm with an H4-type hysteresis loop and a significant apparent BET SSA, attributed to the hierarchical aggregation of nanoparticles into petal like morphology and subsequently into microspheres, potentially enhancing the exposure of electrochemically active sites.[7]

Post Cycling Analysis:

To further study the active material the electrode retrieved post cycling has been subjected to XRD, Raman, XPS and SEM analysis. In XRD analysis (shown in Fig. S16), the major peaks

of NiCo-BDC were observed along with sharp high intense peaks that originated from nickel foam. Whereas, the raman spectra (shown in Fig. S17) reveals similarity between before and after cycling, with peak broadening post cycling which can be attributed to nickel foam. Also, there observed a broad peak between 400 to 600 cm^{-1} which can be attributed to formation of NiO/NiOOH and CoO/CoOOH from reversible reactions during electrochemical studies and also may be due to the thin oxide layer formation over nickel foam.[8,9] This is strongly supported with XPS studies as shown in Fig. S18, where there is slight shift in major peaks towards higher energies which means a greater number of redox species with higher valence leads to increased reaction which ultimately increases the overall performance. The peak at 852.6 eV arises due to nickel foam (Ni^0).[10] From, these observations we can predict that the charge storage mechanism occurs based on reversible reaction between MO and MOOH (where M= Ni or Co). Also, the SEM analysis (shown in Fig. S19) showcases minimal changes in structure and along with other reasons stated earlier, the NiCo-BDC poses excellent electrochemical properties and superior material for supercapacitor applications.
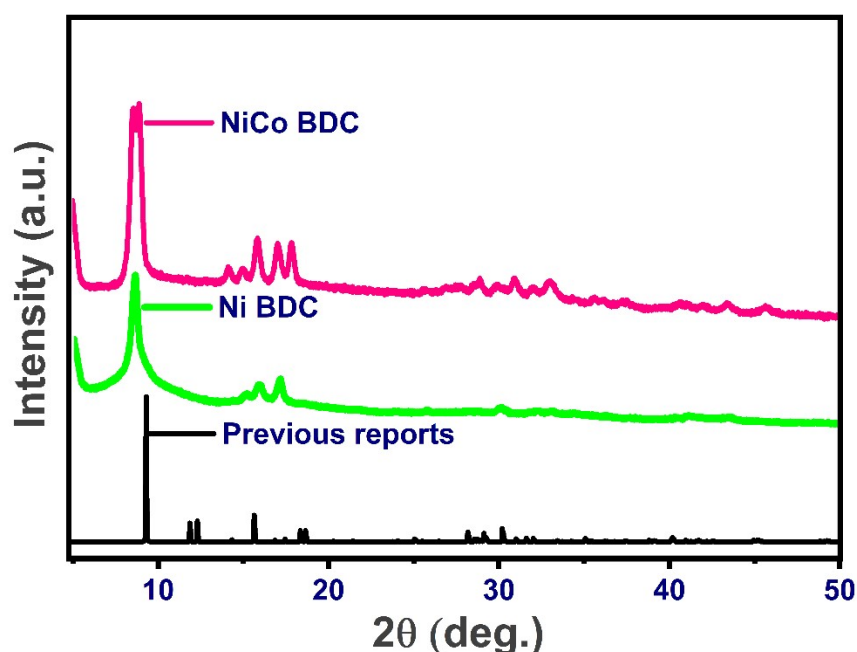
Fig. S2 X-ray diffractogram revealing the similarities between Ni and NiCo-BDC in comparison with previous reports of Ni-BDC.
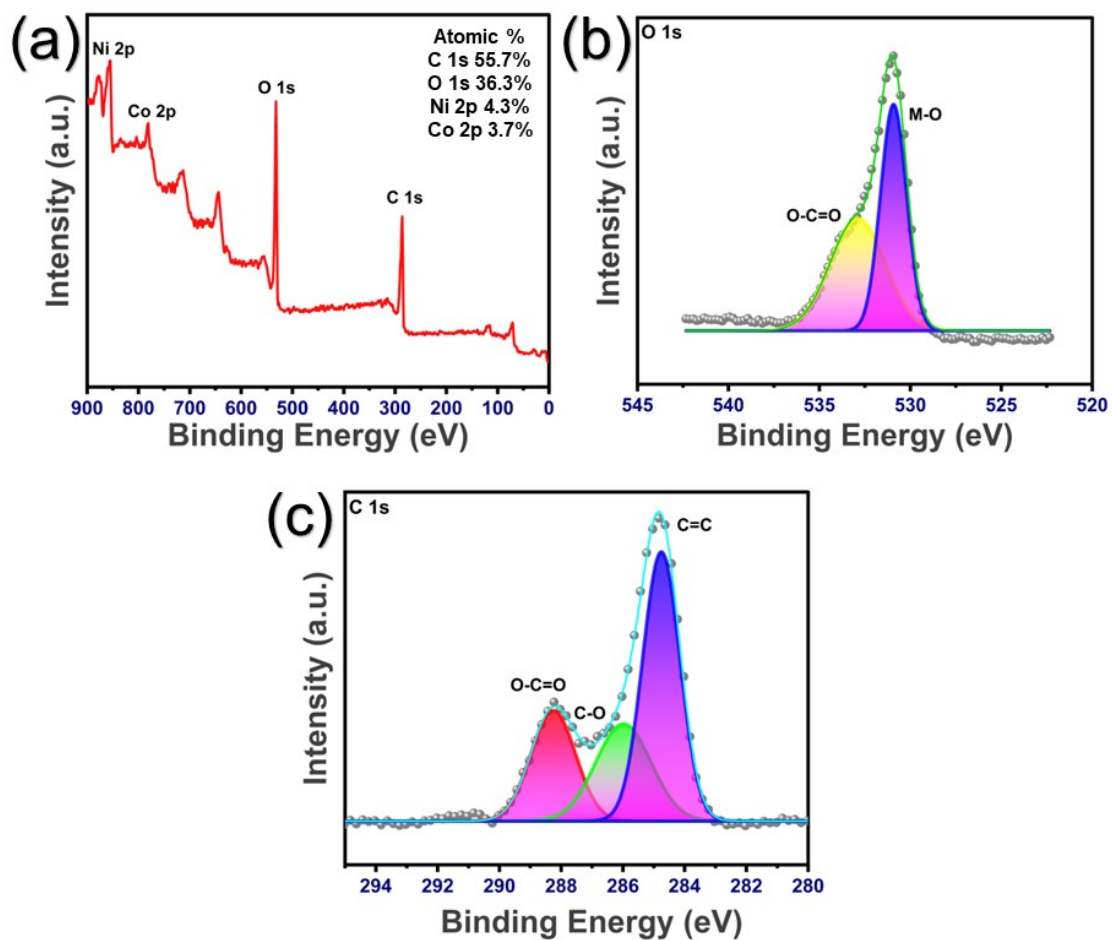
Fig. S3 (a) XPS survey spectra, (b & c) XPS spectra of O and C which shows binding energy for specific bondings.
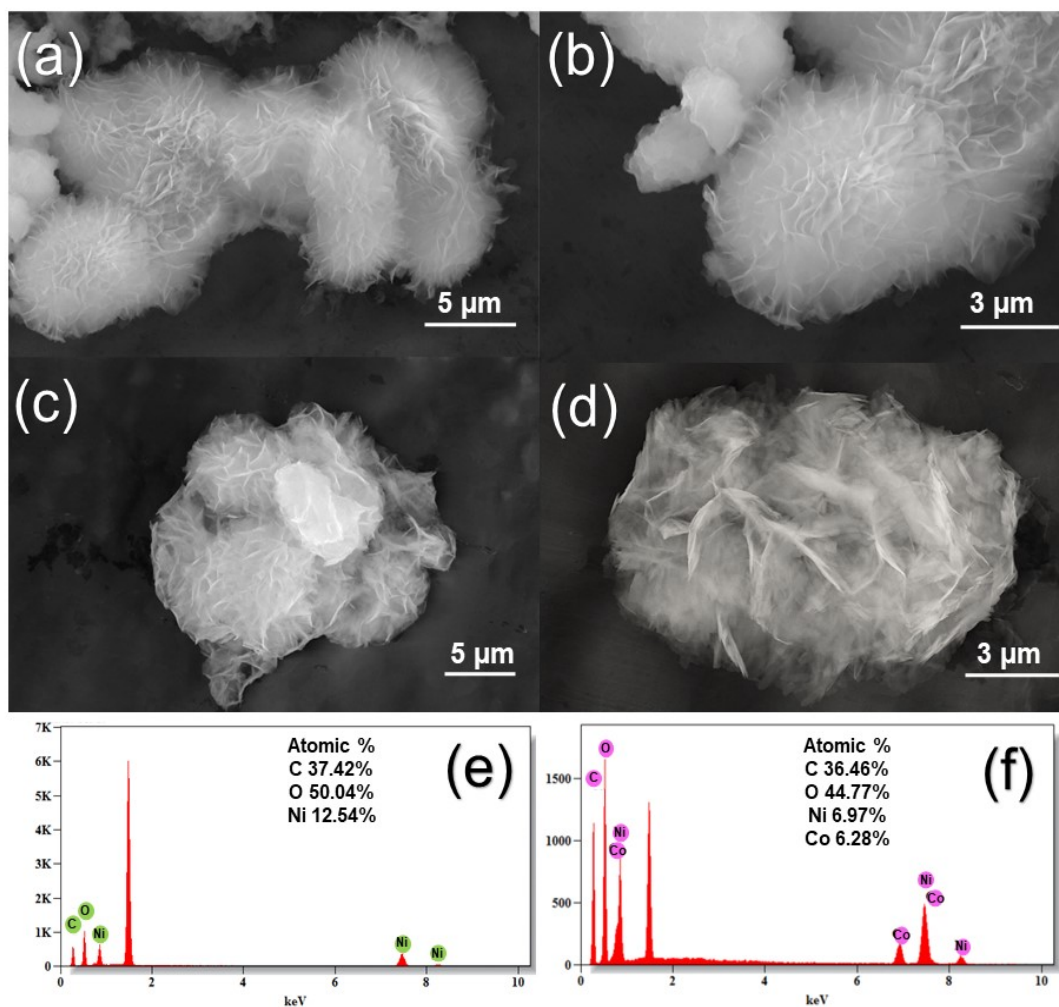
Fig. S4 SEM images and EDS spectra of Ni-BDC (a,b&e) and NiCoBDC (c,d&f).
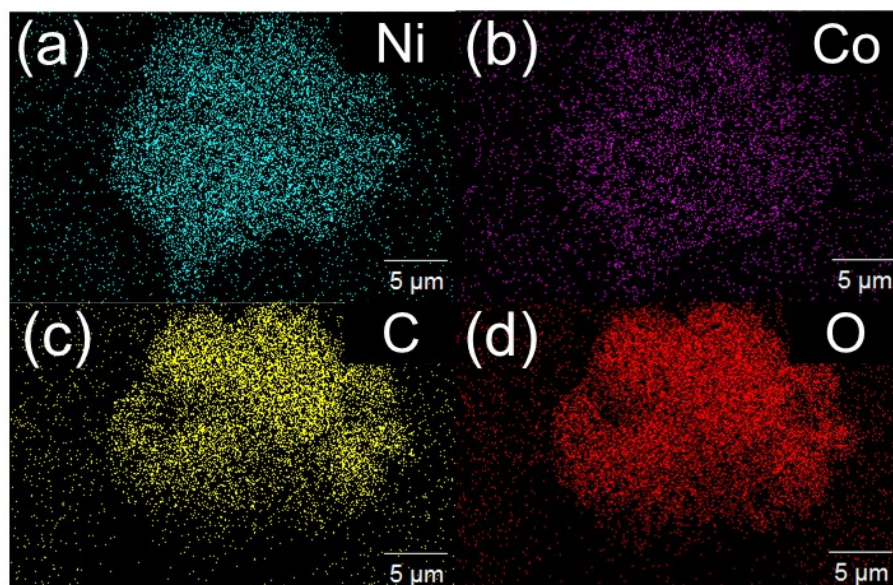

Fig. S5 Showcase the elemental mapping of NiCo-BDC revealing uniformity in presence of various atoms.
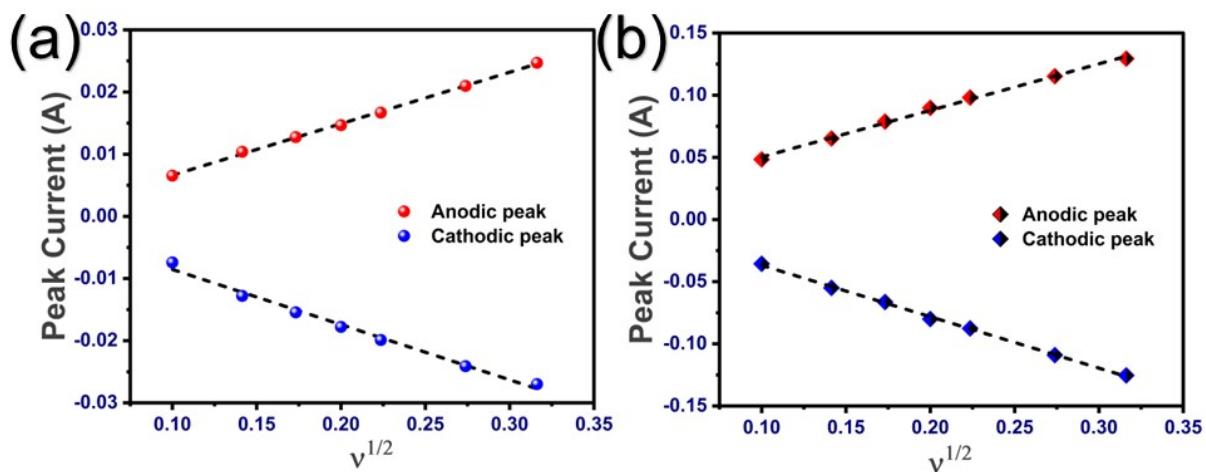
Fig. S6 (a &b) Showcases the relationship between peak current and square root of scan rate which is adopted from Randles-Sevcik equation.
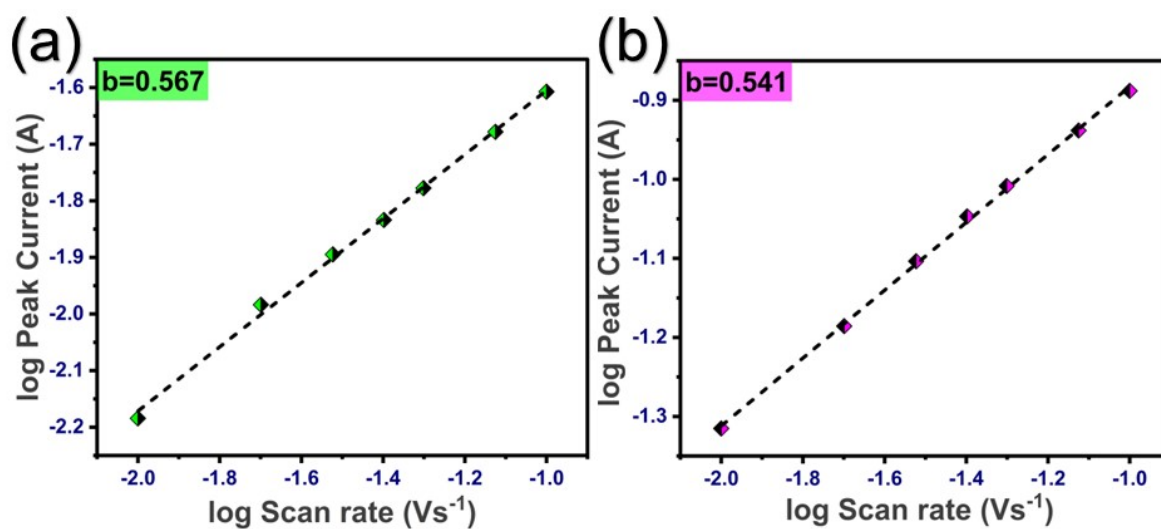

Fig. S7 b-values (slope) calculated from plot between log (i_p) vs. log(υ) for (a) Ni-BDC and (b) NiCo-BDC.
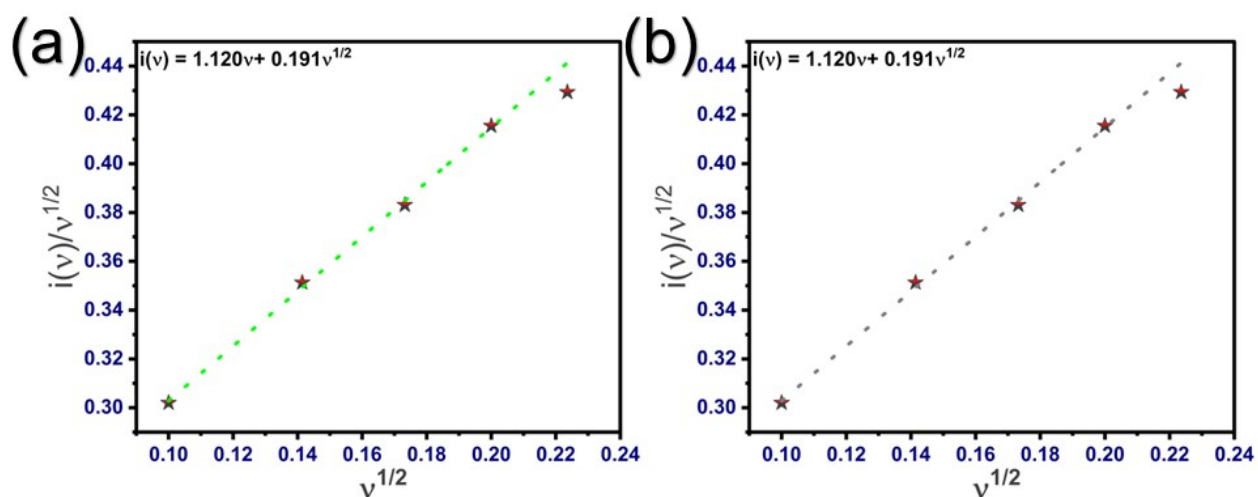
Fig. S8 k_1(slope) and k_2 (intercept) values calculated using Dunn's equation for (a) Ni-BDC and (b) NiCo-BDC.

.
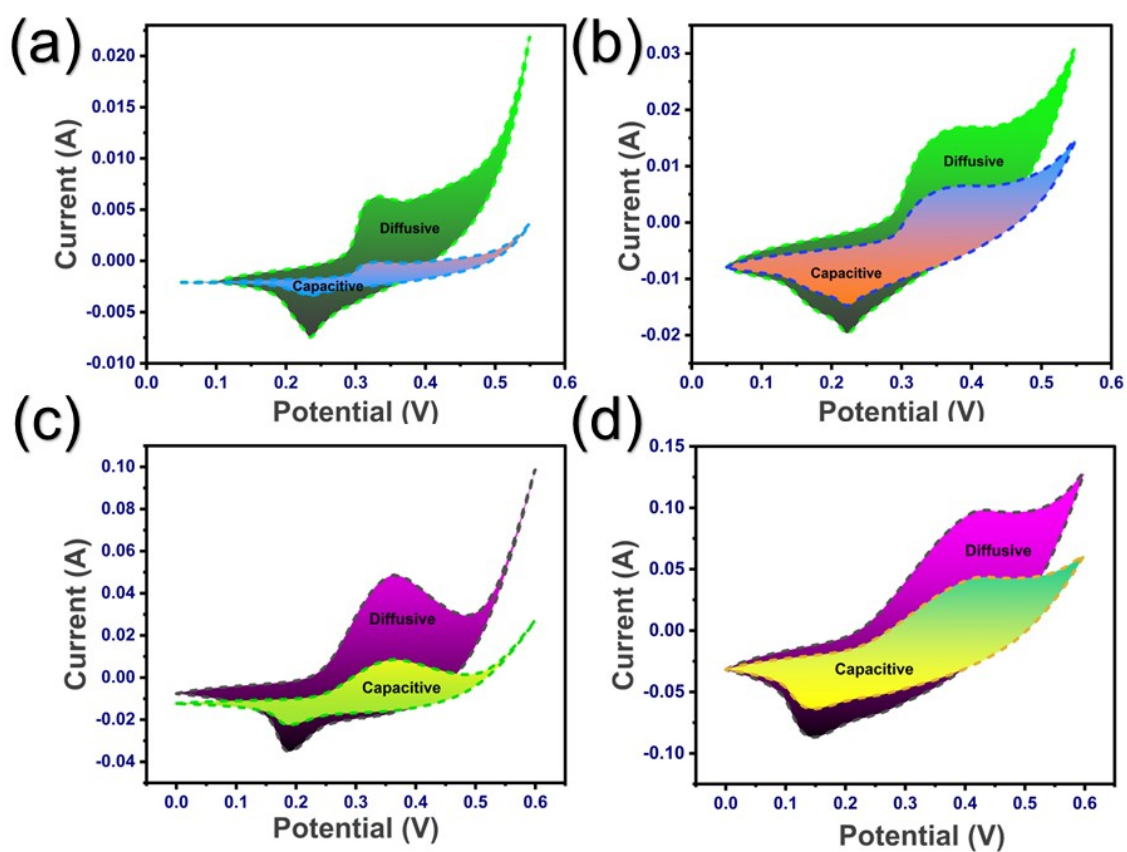
Fig. S9 CV showcasing diffusion and capacitive current contribution for scan rates of 10 (left) and 50 (right) mVs^{-1} for (a) Ni-BDC and (b) NiCo-BDC.
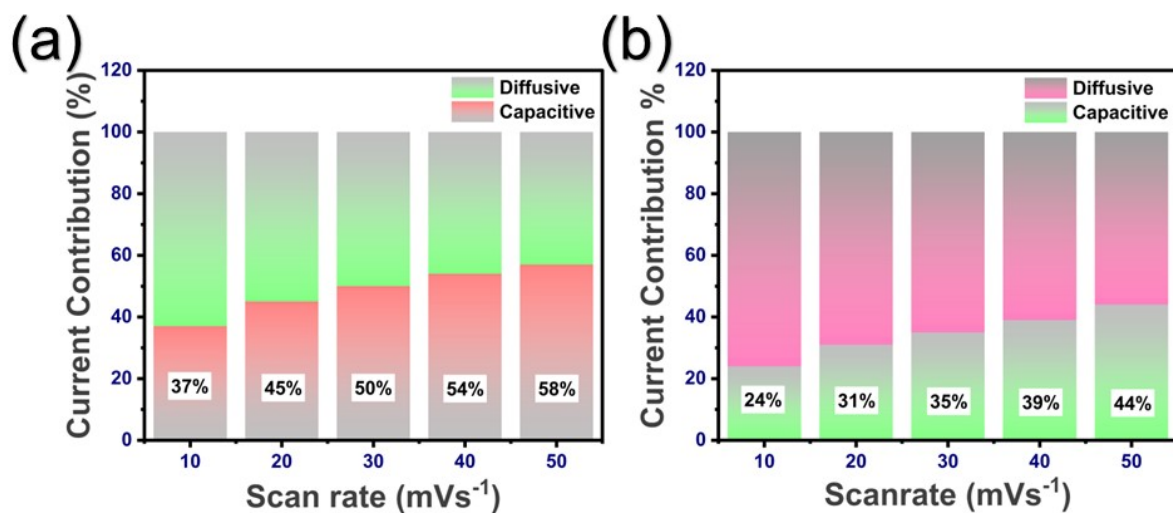
Fig. S10 Current contribution % calculated from Dunn's equation for different scan rates for (a) Ni-BDC and (b) NiCo-BDC.
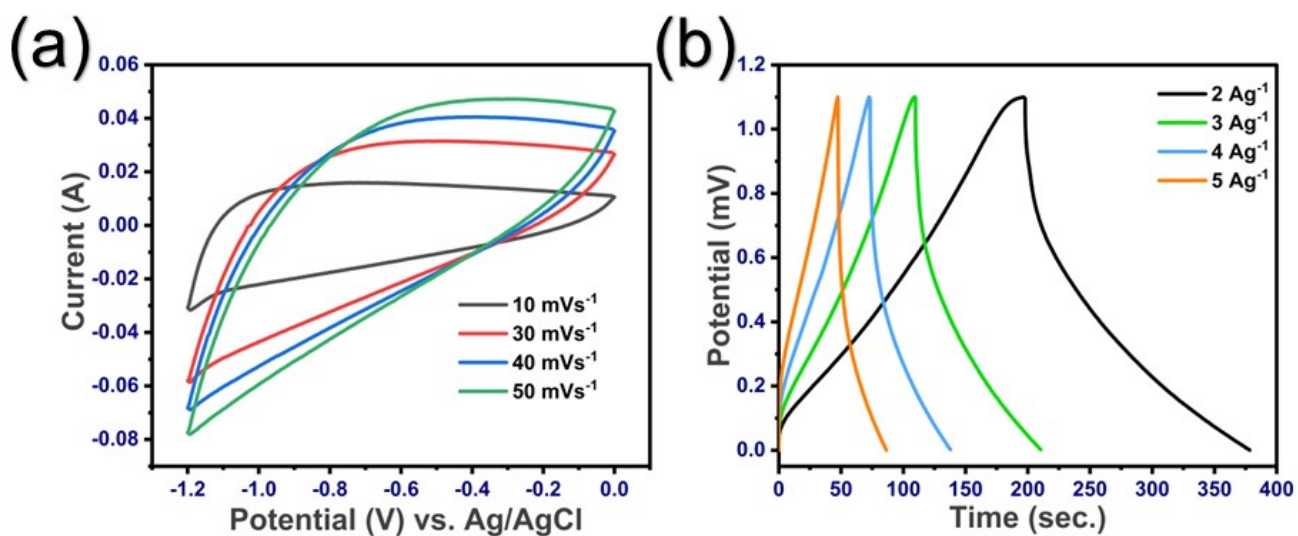
.

Fig. S11 (a) CV curves at different scan rates and (b) GCD curves at different current densities for rGO.
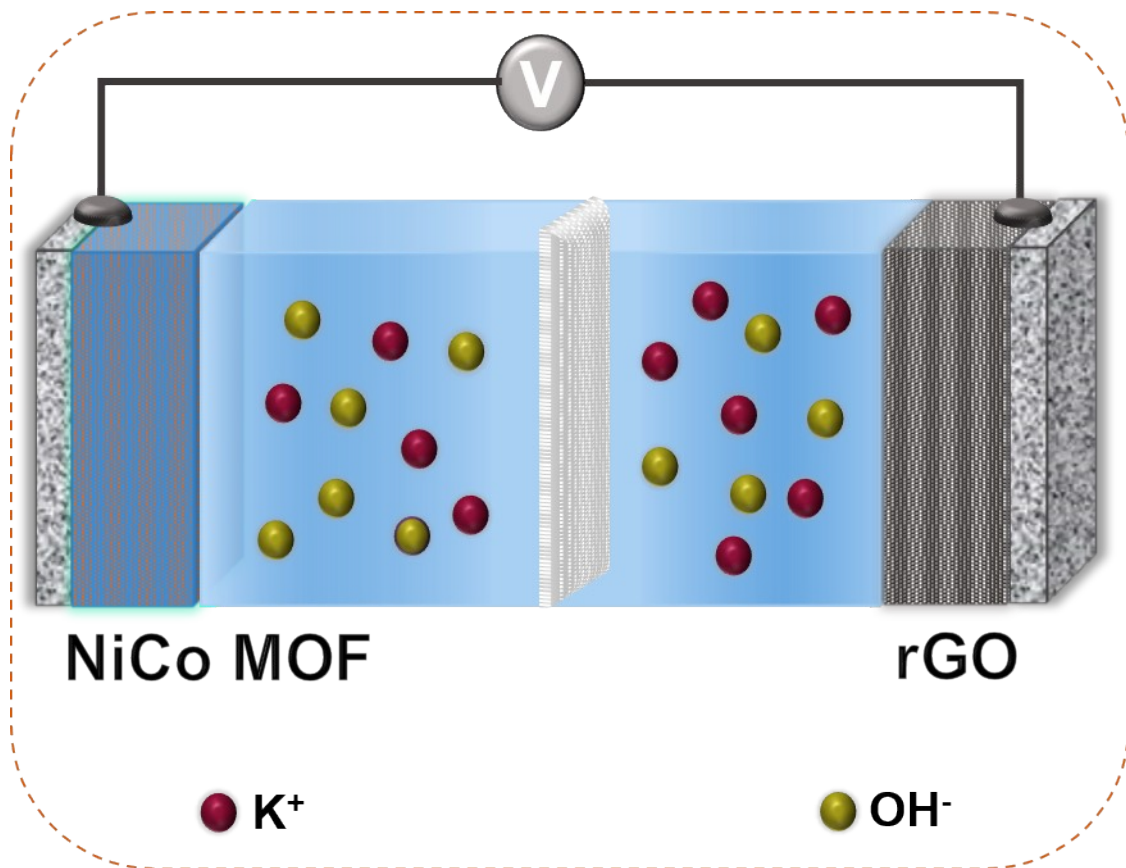
Fig. S12 Schematic of fabricated Aqueous Asymmetric Supercapacitor (AASC).
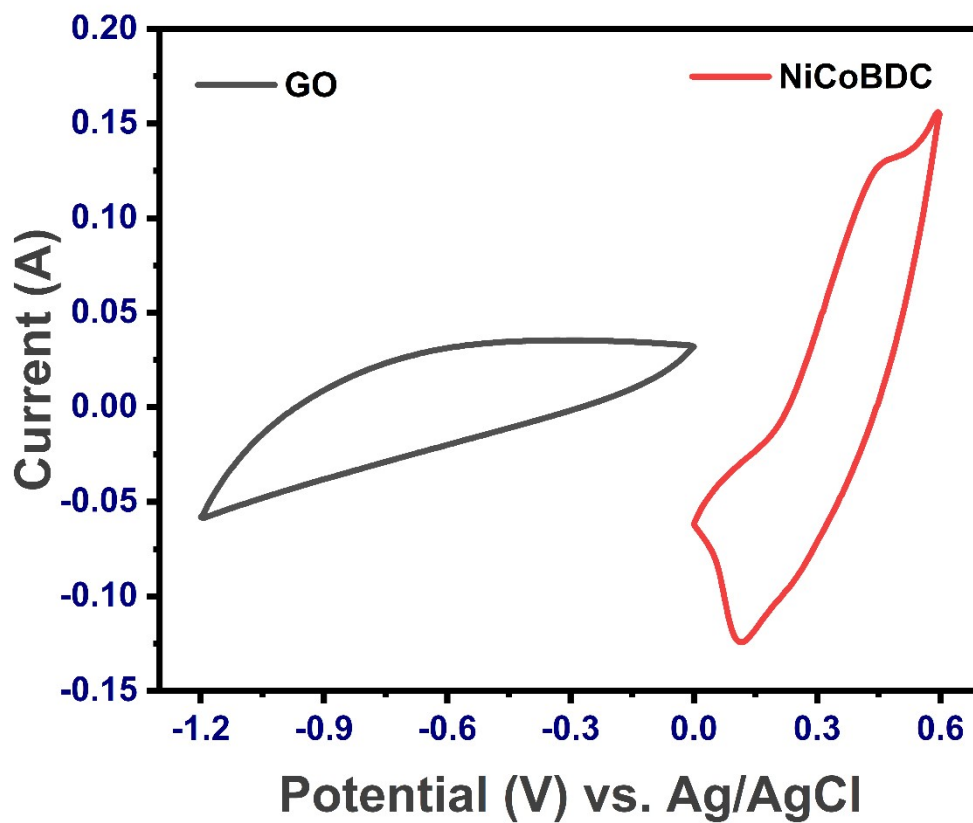
Fig. S13 CV recorded for rGO and NiCo-BDC in three electrode setup separately at 100 mVs^{-1} compared together for knowing the operating voltage of the AASC.
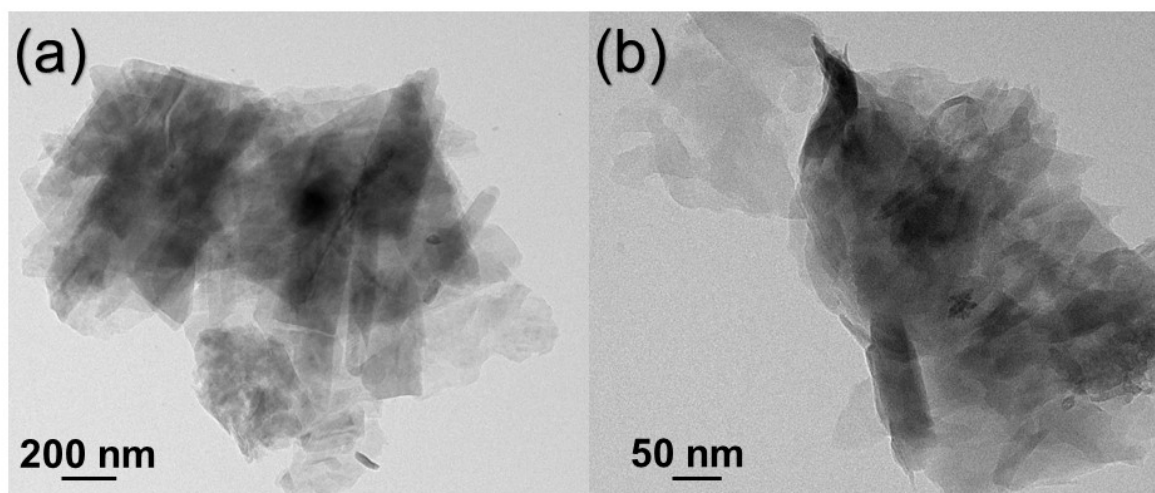

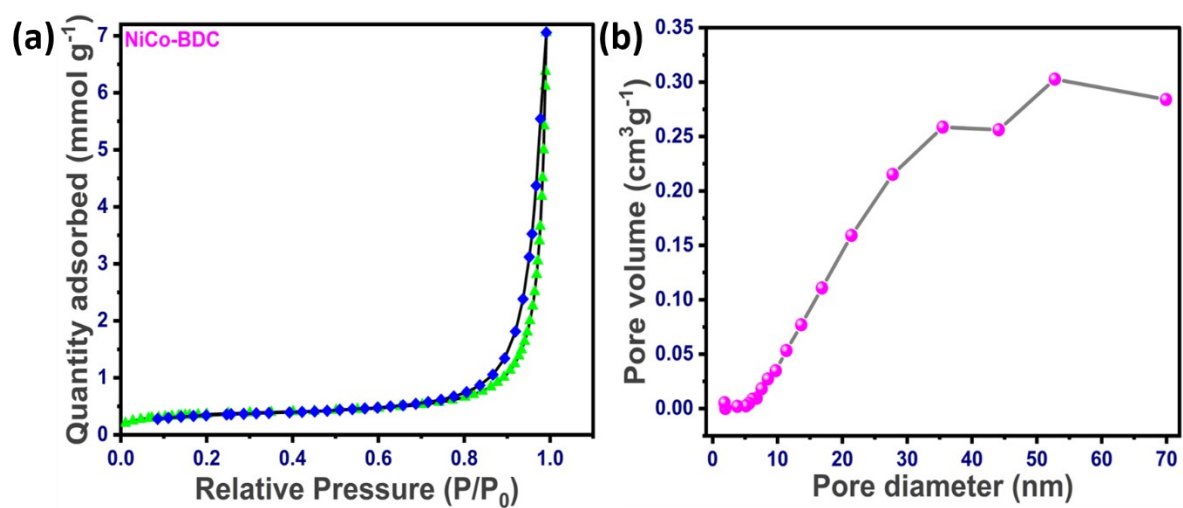**Fig. S14** HR-TEM images revealing a closer view of the nanopetal morphology of the NiCo-BDC.

Fig. S15 N$_2$ adsorption-desorption isotherm of NiCo-BDC and (**b**) pore size distribution determined using BJH method.
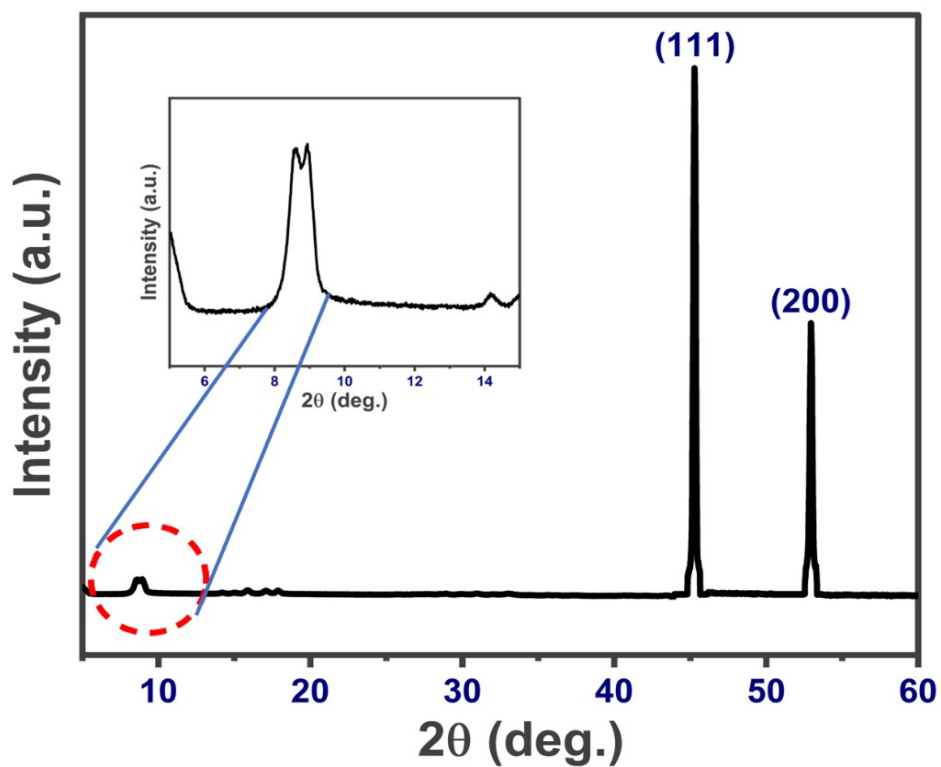

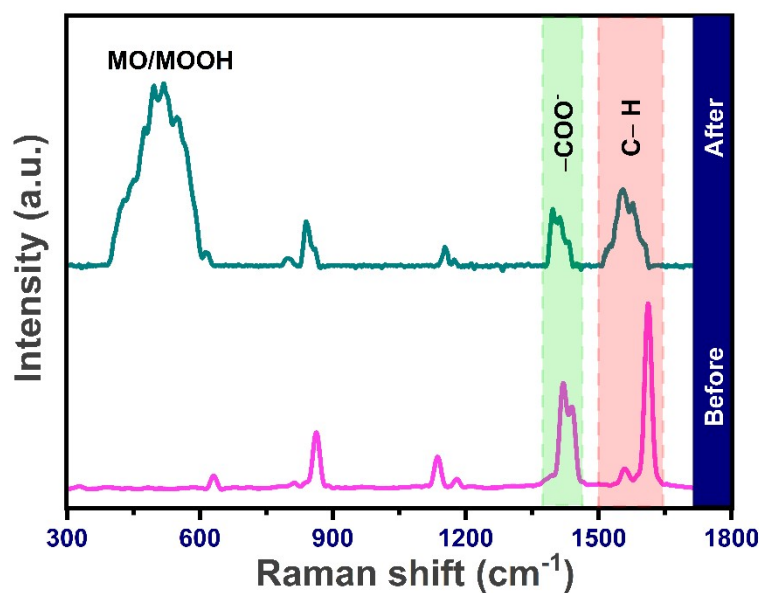**Fig. S16** XRD analysis of NiCo-BDC/NF post cycling.

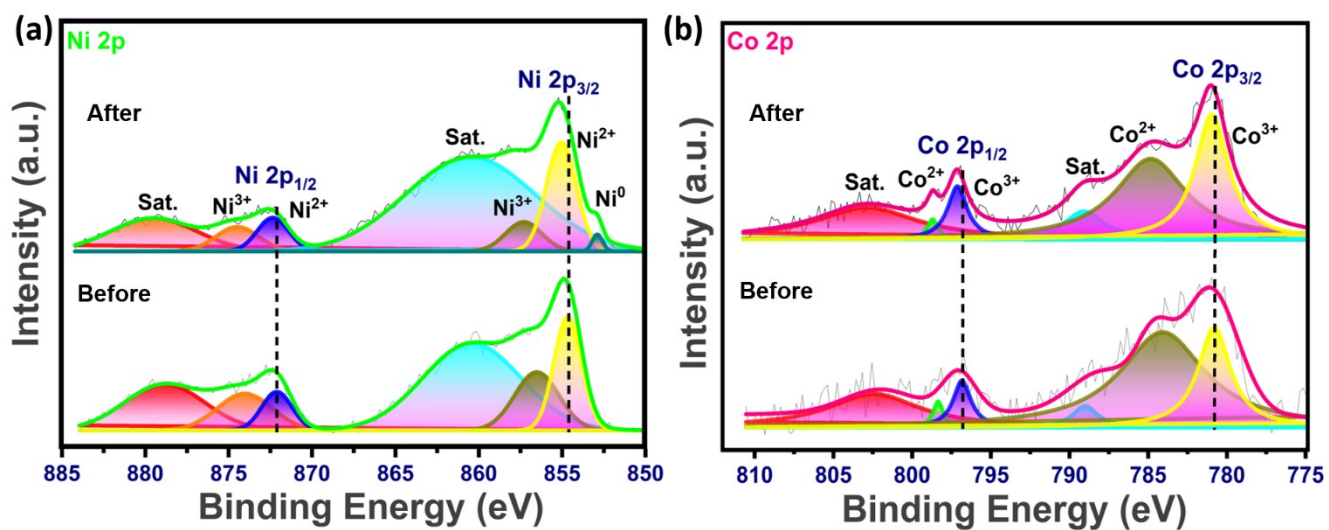**Fig. S17** Comparison between Raman spectra before and after cycling.

Fig. S18 XPS analysis showing comparison between before and after cycling of (a) Ni 2p and (b) Co 2p.
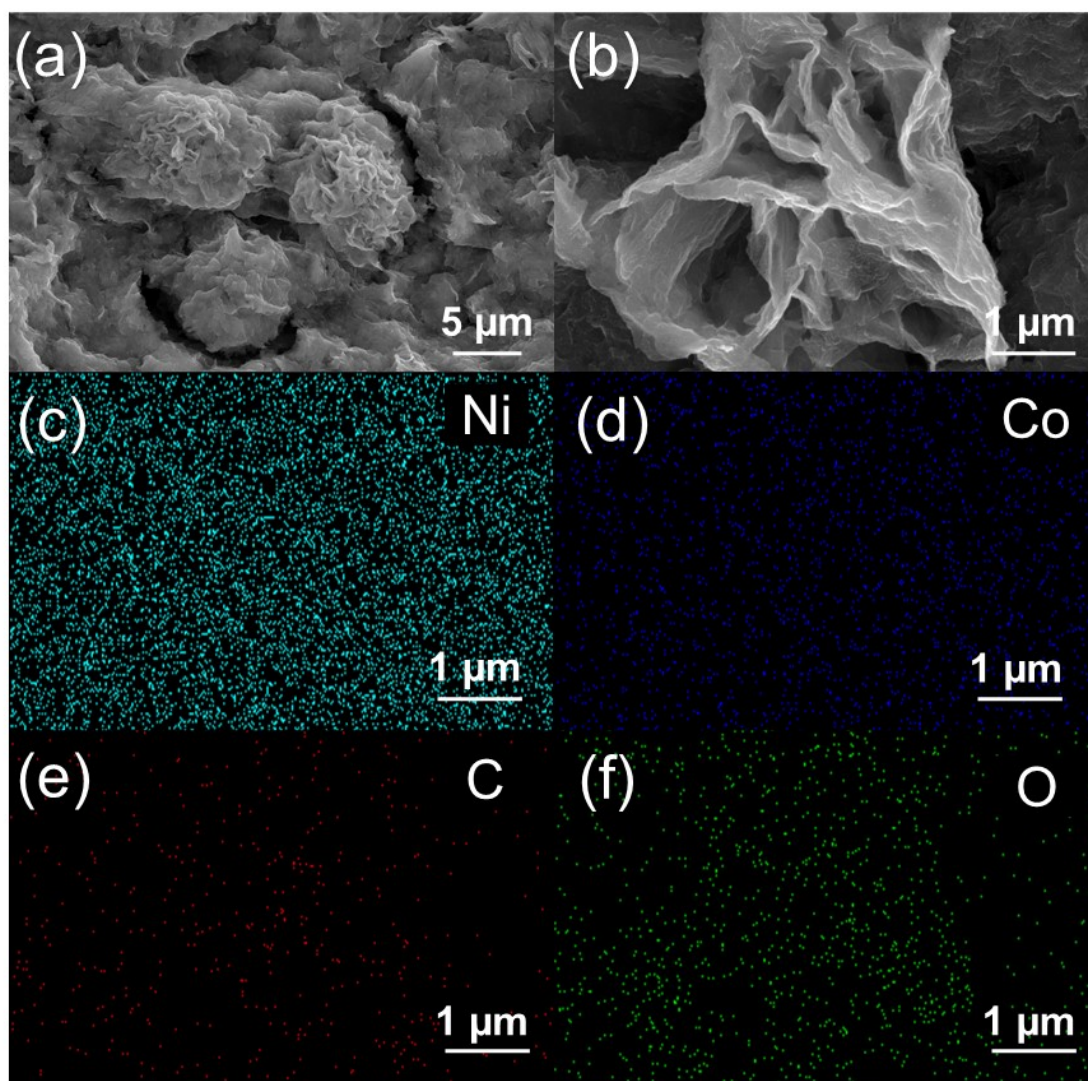
Fig. S19 (a-f) Ex-situ SEM images and elemental mapping of the NiCo-BDC (positive electrode) after 3000 cycles revealing minimum structural damage.
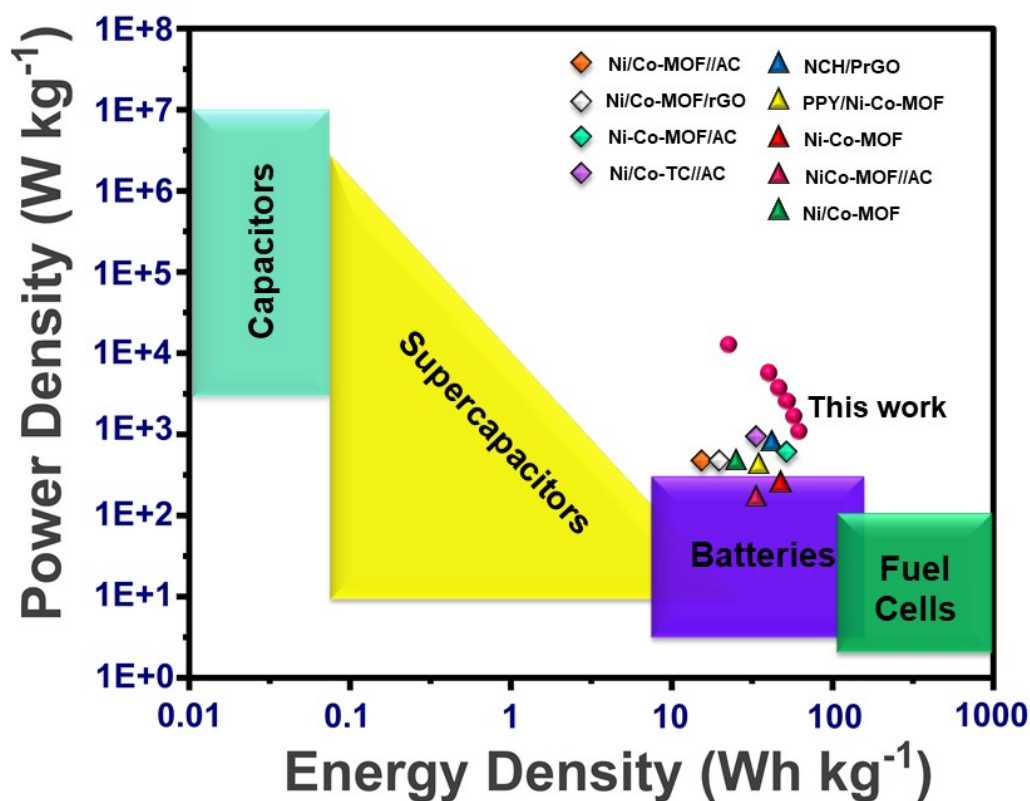

Fig. S20 Ragone plot shows the comparison between various other Ni/Co based MOF and this work.

Active material/Positive electrode	Negative electrode	Energy Density (Whkg^{-1})	Power density (Wkg^{-1})	Ref
Ni/Co-MOF	rGO	42.24	800	11
Ni-Co MOF	AC	77.7	450	12
PPy/Ni-Co-MOF-74	AC	58.4	747.6	13
NCH/PrGO	AC	70.3	900	14
NCMF	AC	50.3	375	7
NiCo MOF/rGO	AC	72.8	850	15
Ni/Co-MOF	AC	20.9	800	16
Ni-Co MOF	AC	55.7	1000	17
Ni/Co-TC	AC	37	801	18
NiCo-BDC	rGO	80	1162	This work

References

1. T. Xiong, W. S. V. Lee and J. Xue, *ACS Appl Energy Mater*, 2018, acsaem.8b01160.
2. A. Hsu, H.-H. Chien, C.-Y. Liao, C.-C. Lee, J.-H. Tsai, C.-C. Hsu, I.-C. Cheng and J.-Z. Chen, *Coatings*, 2018, **8**, 52.
3. X. Fan, H. Xu, S. Zuo, Z. Liang, S. Yang and Y. Chen, *Electrochim Acta*, 2020, **330**, 135207.
4. M. Ghiaci, S. Farahmand, K. Masoomi, M. Safaiee and Jalal. S. Razavizadeh, *Advanced Powder Technology*, 2021, **32**, 660–669.
5. D. Y. Lee, S. J. Yoon, N. K. Shrestha, S.-H. Lee, H. Ahn and S.-H. Han, *Microporous and Mesoporous Materials*, 2012, **153**, 163–165.
6. S. A. Patil, P. K. Katkar, M. Kaseem, G. Nazir, S.-W. Lee, H. Patil, H. Kim, V. K. Magotra, H. B. Thi, H. Im and N. K. Shrestha, *Nanomaterials*, 2023, **13**, 1587.
7. Surya. V. Prabhakar Vattikuti, N. To Hoai, J. Zeng, R. Ramaraghavulu, N. Nguyen Dang, J. Shim and C. M. Julien, *Materials*, 2023, **16**, 2423.
8. X. Yang, H. Zhang, W. Xu, B. Yu, Y. Liu and Z. Wu, *Catal Sci Technol*, 2022, **12**, 4471–4485.
9. T. M. Masikhwa, M. J. Madito, D. Momodu, A. Bello, J. K. Dangbegnon and N. Manyala, *J Colloid Interface Sci*, 2016, **484**, 77–85.
10. Y.-J. Shih, Y.-H. Huang and C. P. Huang, *Electrochim Acta*, 2018, **263**, 261–271.
11. X. Zhang, J. Wang, X. Ji, Y. Sui, F. Wei, J. Qi, Q. Meng, Y. Ren and Y. He, *J Alloys Compd*, 2020, **825**, 154069.
12. C. Ye, Q. Qin, J. Liu, W. Mao, J. Yan, Y. Wang, J. Cui, Q. Zhang, L. Yang and Y. Wu, *J Mater Chem A Mater*, 2019, **7**, 4998–5008.
13. Y. Cao, N. Wu, F. Yang, M. Yang, T. Zhang, H. Guo and W. Yang, *Colloids Surf A Physicochem Eng Asp*, 2022, **646**, 128954.
14. K. Z. Mousaabadi, A. A. Ensafi, E. Naghsh, J.-S. Hu and B. Rezaei, *Sci Rep*, 2023, **13**, 12422.
15. M. S. Rahmanifar, H. Hesari, A. Noori, M. Y. Masoomi, A. Morsali and M. F. Mousavi, *Electrochim Acta*, 2018, **275**, 76–86.
16. S. Gao, Y. Sui, F. Wei, J. Qi, Q. Meng, Y. Ren and Y. He, *J Colloid Interface Sci*, 2018, **531**, 83–90.
17. M. G. Radhika, B. Gopalakrishna, K. Chaitra, L. K. G. Bhatta, K. Venkatesh, M. K. Sudha Kamath and N. Kathyayini, *Mater Res Express*, 2020, **7**, 054003.
18. H. Mei, Y. Mei, S. Zhang, Z. Xiao, B. Xu, H. Zhang, L. Fan, Z. Huang, W. Kang and D. Sun, *Inorg Chem*, 2018, **57**, 10953–10960.